ORIGINAL RESEARCH ARTICLE

Effect of Furnace Parameters on Optical Emission Spectra of Hematite Reduction by Hydrogen Plasma

HENNA-RIIKKA PUTAALA, HENRI PAUNA, AREEJ JAVED, UBAID MANZOOR, DENNIS KLAPPROTH, ISNALDI R. SOUZA FILHO, VILLE-VALTTERI VISURI, ANUMOY GANGULY, MARKO HUTTULA, TIMO FABRITIUS, and DIERK RAABE

Hydrogen plasma smelting reduction (HPSR) has been envisaged as a potential CO_2-lean process for ore-based steelmaking, combining the reduction, melting and refining steps into a single unit process. However, scaling the process to industrial use still requires some work. In previous studies, optical emission spectroscopy (OES) has been suggested as a potential process monitoring method for HPSR. The present study investigates the effect of furnace parameters, such as the arc length and current, on the optical emissions of the hematite reduction by HPSR. To understand the effect of slag components, a few experiments were also conducted with fluxed hematite. It was found that the optical emissions of non-ionized elements are more intense at lower currents than at higher currents due to a lower level of ionization. The electron density calculated from the optical emissions could be used to estimate the arc length if the arc cannot be directly observed. It was also noted that the optical emissions of the slag components are very distinct in fluxed hematite experiments, which is of interest for potential industrial applications. Finally, the positioning of the optical fiber in relation to the plasma was found to be crucial for the successful monitoring of the experiments.

https://doi.org/10.1007/s11663-025-03552-5

I. INTRODUCTION

STEEL is a durable and long-lasting material which can be used for countless applications. As the world continues to move towards a more sustainable future, steel demand is expected to continue its rise in the coming decades.[1] However, currently the steel industry accounts for approximately 7 pct of the total anthropogenic CO_2 emissions worldwide.[2,3] Steel is produced predominantly either from iron ore using the integrated blast furnace-basic oxygen furnace (BF-BOF) route, or from scrap in electric arc furnaces (EAFs). The average emissions for global steel production are about 1.91 tons CO_2 per ton of steel produced.[4] Most of this is caused by the integrated BF–BOF route, while scrap-based production has much lower direct CO_2 emissions per tonne of produced steel.[5] However, since the lifecycle of steel is very long, for instance up to 20 years for vehicles and up to 100 years for buildings,[6,7] the amount of recycled steel cannot by itself satisfy the increasing need for steel in the future decades.[8] Consequently, new CO_2-lean reduction methods are crucially needed for ore-based primary steel production.

Over the past decades, hydrogen has been studied as a reducing agent to replace coke in ironmaking. The demand for hydrogen-based steel is expected to reach 660 Mt by 2050.[9] Hydrogen direct reduction (H-DR) is one method in which iron ore is reduced in the solid state with hydrogen gas to produce direct reduced iron (DRI). For this purpose, shaft furnaces and fluidized bed reactors have been proposed.[10] Two routes have been envisioned for the further processing of DRI: (1) melting in an electric arc furnace and (2) smelting in an electric smelter followed by refining in a basic oxygen furnace (BOF).[1,11,12] Alternatively, both the reduction and smelting could be done in a single step using hydrogen plasma smelting reduction (HPSR), an emerging technology in which the ore is exposed to a plasma arc consisting of hydrogen and stabilizing gas, most commonly argon. Souza Filho *et al.*[13] demonstrated the

HENNA-RIIKKA PUTAALA, HENRI PAUNA, AREEJ JAVED, VILLE-VALTTERI VISURI, and TIMO FABRITIUS are with the Process Metallurgy Research Unit, University of Oulu, P.O. Box 4300, 90014 Oulu, Finland. Contact e-mail: henna-riikka.putaala@oulu.fi UBAID MANZOOR, DENNIS KLAPPROTH, ANUMOY GANGULY, and DIERK RAABE are with the Max Planck Institute for Sustainable Materials, Max-Planck-Str. 1, 40237 Düsseldorf, Germany. ISNALDI R. SOUZA FILHO is with the Max Planck Institute for Sustainable Materials and also with the Institut Jean Lamour, Université de Lorraine, 2 allée André Guinier, 54011 Nancy, France. MARKO HUTTULA is with the Nano and Molecular Systems Research Unit, University of Oulu, P.O. Box 3000, 90014 Oulu, Finland.

Manuscript submitted December 16, 2024; accepted April 6, 2025.

Published online: 28 April 2025

combination of H-DR and HPSR in their recent study, where the hematite pellets were first reduced in H-DR and then further processed in HPSR to create a hydrogen-efficient and stable reduction process. The effect of pre-reduction degree on HPSR reduction behavior and other process-related parameters was studied by Ernst *et al.*[14] They found that a high oxygen content in the ore predicts high hydrogen utilization and therefore a fast reduction progression.

The stability of the plasma in HPSR is one key factor for the possible future operation of industrial-scale furnaces. Zarl *et al.*[15] determined stability fields for HPSR by arc length, current and voltage for different gas compositions with and without iron ore charging. The charging of iron ore was found to significantly decrease the stability, whereas argon acted as a stabilizer in the process. Therefore, if continuous charging of the input material is used, the charging process should be optimized. Optimal charging rates of the material were further studied by Zarl *et al.*[16] and Ernst *et al.*[17] They concluded that a high iron ore charging rate with a low hydrogen concentration during the charging phase increases the hydrogen utilization but decreases the reduction rate, resulting in a high oxygen removal rate after the reduction phase and therefore short process times. Considering the efficient use of hydrogen, Souza Filho *et al.*[18] found that decreasing the hydrogen percentage in both the total pressure and the molar fraction of the input gas results in increased hydrogen utilization. Reducing the pressure and fraction of hydrogen in the input gas is also favorable to the efficient use of hydrogen.

Hematite has previously been studied as an input material for HPSR. Naseri Seftejani *et al.*[19] studied several process parameters related to the reduction of hematite. They found that the utilization of the injected hydrogen was high at the beginning of the process and decreased with the decreasing amount of iron oxide in the melt. They also noted that the high basicity of the slag decreased the phosphorus content in the iron produced. In another study, different basicities of slag were further studied by Naseri Seftejani *et al.*[20] They found the optimal short basicity of the slag (B_2 = pct CaO/pct SiO_2 = 2.3) for the reduction and hydrogen utilization, and concluded that although hydrogen utilization decreased with time in batch-charged experiments, it remained almost constant during continuous charging experiments. The reduction kinetics of hematite was studied by Souza Filho *et al.*,[21] who concluded that it depends on the relation of the sample mass to the energy input of the arc. For an optimized input mass with respect to the arc power, the reduction was completed in 15 minutes. Recently, Kannan *et al.*[22] studied the reduction behavior of hematite in powder form, and found that using the powder form leads to an about 10 times faster reaction kinetics compared to previous studies with hematite pellets, even with a fraction of hydrogen being 5 times lower (Ar + 2 pct H_2) in the input gas in this specific experiment. These findings suggest that the effect of particle size should therefore be considered when planning future experiments with hematite.

Several studies have recently investigated the use of HPSR for reducing low-quality ores and sidestream materials from other processes. Jovičević-Klug *et al.*[23] used red mud, a toxic waste from aluminum production, as a feedstock for HPSR. After 10 minutes of reduction, they achieved 70 pct metallization with only 7 pct of iron lost through evaporation. By further processing the oxide portion with suitable extraction methods, the extraction of rare-earth metals, such as Sc and Y, would be possible. They proved that HPSR would be a sustainable and economically feasible method for turning red mud into valuable metals in a carbon-lean way. Nickel leaching residue was reduced by Zulhan *et al.*,[24] who were able to reduce the iron in only 30 seconds exposure to Ar + 80 pct H_2, although to reduce the sulfur content in the metal below 0.1 pct, an operation time of 180 seconds was required. Büyükuslu *et al.*[25] used HPSR with the gas composition Ar + 10 pct H_2 at an absolute pressure of 0.9×10^5 Pa to reduce a low-grade hematite ore containing phosphorus. They achieved 95 pct dephosphorization after 5 minutes of exposure to the plasma. All of these studies show that HPSR is an effective method to reduce low-grade ores, sidestream materials and even toxic waste materials for sustainable steel production.

The challenge with the process monitoring of the HPSR process is that industrial-scale furnaces do not always offer enough space for a video camera or similar visual observation methods. Therefore, the plasma arc and the molten pool must be observed by other means. Optical emission spectroscopy (OES) has been proven to be suitable for the monitoring of the EAF process,[26–28] so due to the similarities between the two processes, OES may also be suitable for the HPSR process monitoring. Some studies have already been conducted on the use of OES for monitoring the HPSR process.[29,30] They have shown that OES can be used to obtain information on the composition of the plasma, plasma temperature and electron density, as well as the position of the plasma on the crucible in laboratory- and pilot-scale furnaces.

The aim of this article is to provide further information on the analysis of OES spectra in HPSR processing of pure and slag-fluxed hematite. We study how furnace-related parameters, such as arc length d and current I, affect optical emission spectra in pure hematite HPSR experiments and how the addition of slag-formers changes the effect. Plasma temperature and electron density are also determined from the optical spectra. Furthermore, the spectra are compared to video frames of the plasma to determine whether a correlation between certain colored pixels and emission line intensities can be found.

II. MATERIALS AND METHODS

The measurements were conducted at Max Planck Institute for Sustainable Materials (formerly Max Planck Institute for Iron Research) using a continuous-flow arc-melting AM200 reactor. The volume of the furnace was 18 L.[13,18,21] An image of the furnace is presented in Figure 1.

The spectra were measured with an Avantes 3-channel spectrometer. The equipment used to record the spectra consisted of a spectrometer, a computer to adjust the settings of the spectrometer, and an optical fiber looking into the furnace. The spectrometer measures electromagnetic radiation in three wavelength ranges: ultraviolet (UV, 195.336 to 469.460 nm), visible (VIS, 439.969 to 684.669 nm) and near-infrared (NIR, 666.046 to 1015.360 nm). The integration times can be individually adjusted for each of the channels. The spectrometer automatically merges the channels, creating a continuous spectrum that covers the entire wavelength range, which was used in this study. However, only UV and VIS channels were recorded due to a fracture in one of the optical fibers during shipping.

The videos were recorded with a Canon EOS 6D camera (frame rate 24 ps, shutter speed 1/50, ISO 2000, aperture F3.2), which was positioned to look into the furnace horizontally. A piece of sunfoil from Teknofokus Ltd. was placed on the lens to protect the camera from saturation due to the extreme brightness of the plasma. Both the optical fiber and the video camera were supported so that they were steady during the measurements.

A. *Materials*

The materials to be tested included pure hematite (Fe_2O_3) as well as hematite fluxed with 5 wt pct SiO_2, 3 wt pct CaO, and 2 wt pct Al_2O_3 (short basicity $B_2 = 0.6$). The SiO_2–Al_2O_3 content of the fluxed hematite compared to ores from other studies is presented in Figure 2.

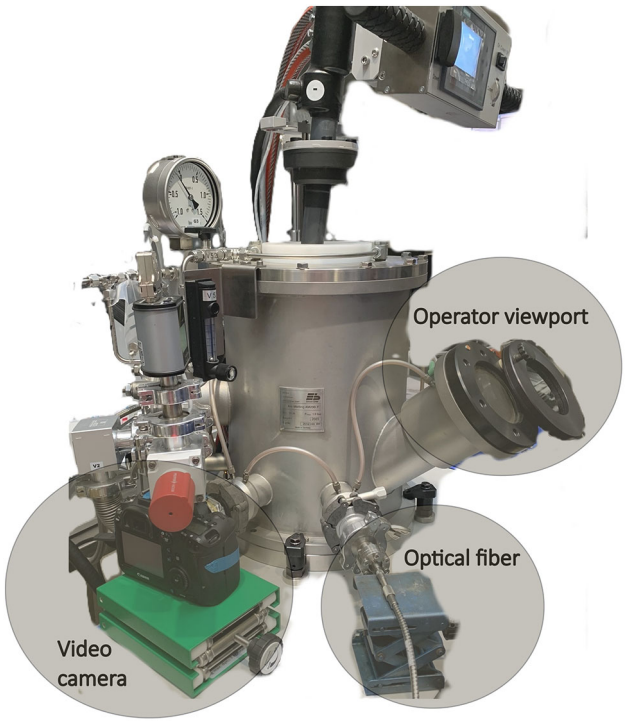

Fig. 1—The furnace with the view ports for the video camera and the optical fiber. Above the optical fiber feed-through is the view port for the furnace operator.

The figure shows that the composition of the fluxed hematite used in this study compares well with the compositions of other ores from literature, which were compiled by Muwanguzi *et al.*[31] Thus, these oxides are typical impurities in iron ores, which is why their behavior in OES spectra was of interest in this study. Slag-forming agents are also relevant for the quality of steel produced in industrial-scale HPSR furnaces in the future, when phosphorus and sulfur need to be removed from the metal, so their respective reaction and partitioning behavior during the process should be well monitored and understood. The sample size was 15 g in all experiments. The experimental parameters are presented in Table I.

First, the sample was weighed and compressed into a single cylinder-shaped compact (diameter 2 cm, height 1.5 cm) to prevent the fine powder from blowing off the crucible when the plasma arc hits it. The sample was then loaded onto the copper crucible, after which the furnace chamber was closed and vacuum pumped. The chamber was then filled with 90 pct argon and 10 pct hydrogen up to the pressure of 1 bar, and a flow rate of 5 L/min was applied. The plasma arc was ignited between the tungsten electrode and the copper crucible and then moved on top of the sample. The electrode was manually moved by the operator during the

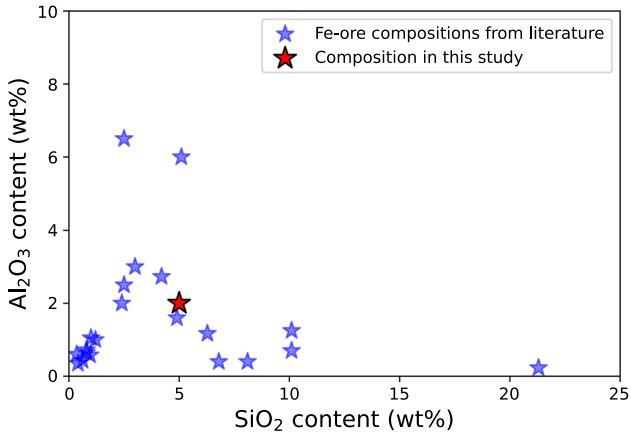

Fig. 2—Comparison of the SiO_2 *vs* Al_2O_3 content of the fluxed hematite used in this study and the numeric data from literature compiled by Muwanguzi *et al.*[31]

Table I. Experimental Parameters

Experiment	Material	Current *I* (A)	Arc Length *d* (mm)
1	hematite	100	10
2	hematite	200	10
3	hematite	100	5
4	hematite	200	5
5	hematite	100	15
6	hematite	200	15
7	hematite + slag	200	5
8	hematite + slag	200	10
9	hematite + slag	200	15

experiments. The experiments were carried out in steps of 2.5 minutes, and after each step the dust and reaction gases were removed from the chamber by vacuum pumping and the chamber was filled again with new reaction gases. In these experiments, there were a total of five 2.5 minutes steps, so the total reduction time was 12.5 minutes for each experiment. After the experiment, the furnace chamber was opened and the chamber and the crucible were cleaned. No significant erosion or ablation of the tungsten electrode was observed during the experiments.

B. *Optical Emission Spectroscopy and Plasma Analysis*

The spectra were analyzed with MATLAB. First, the merged spectra needed to be normalized with respect to the integration time of each spectrometer channel. This was done by dividing the spectra by the integration times. In the overlapping regions between UV/VIS and VIS/NIR, a linear fit of the integration times was constructed, and the spectrum was divided by it.

The high energy of the plasma is absorbed by the atoms, ions and molecules in the plasma, which excites their electrons into discrete higher energy states. As the respective species in their higher energy states fall back into likewise discrete lower energy states, the excess energy is emitted as a photon. The energy E of this photon is characteristic of the element and energy state in question, and can be converted to wavelength λ according to Planck's relation (Eq. [1])

$$E = \frac{hc}{\lambda}, \qquad [1]$$

where h is Planck's constant and c is the speed of light in vacuum. This means that the emissions of different elements can be distinguished from each other in terms

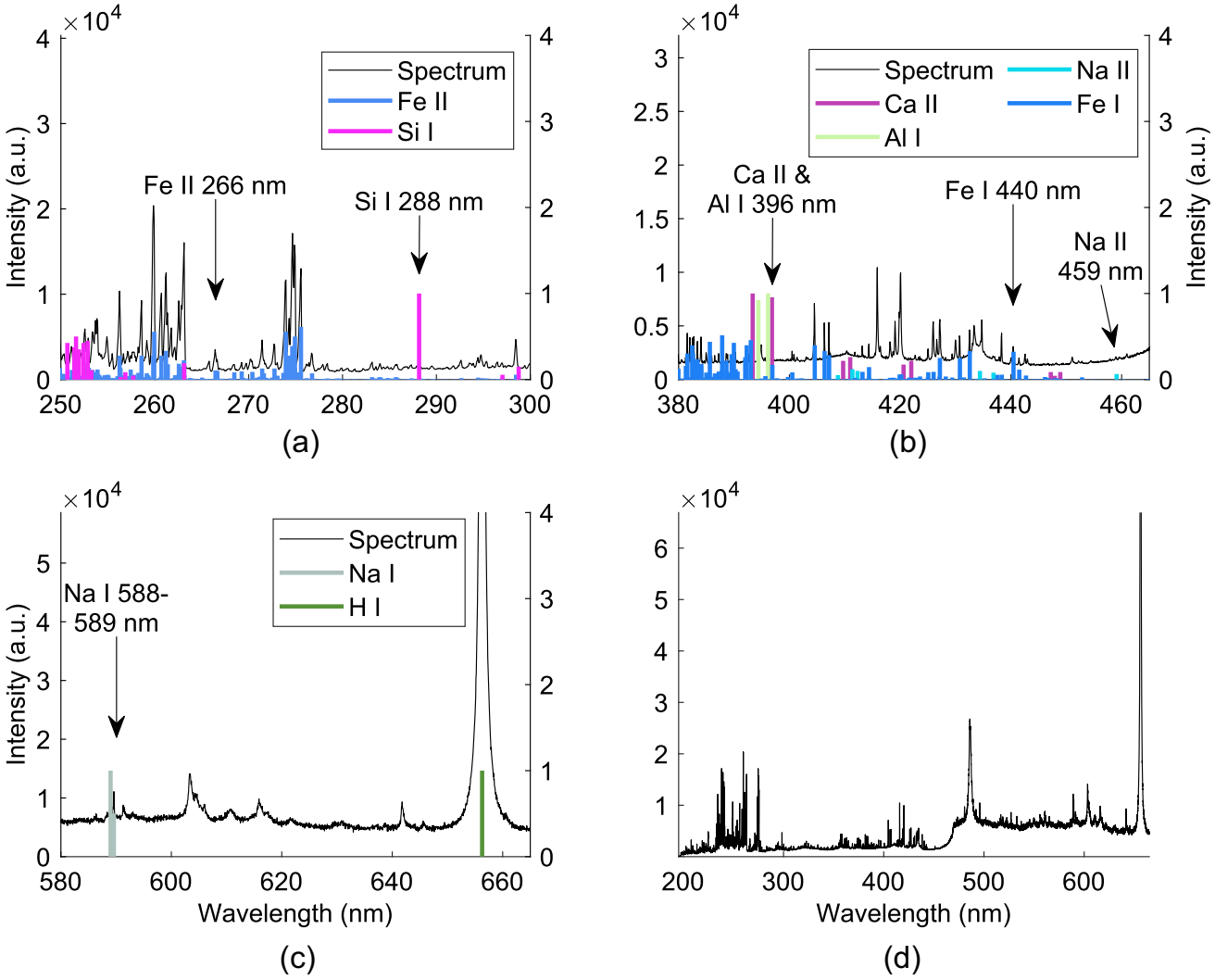

Fig. 3—An example of using the NIST reference wavelengths to find the correct emission lines. The emission lines used in this work are marked in the plots (*a*) through (*c*) by arrows. The entire recorded spectrum without the NIST reference wavelengths is shown in (*d*). Note that the base level of the VIS range is higher than the base level of the UV range due to the normalization by integration times.

of their respective wavelength spectra. Therefore, the intensity of the recorded spectra is conveniently presented as a function of wavelength. The emission lines are labeled as the symbol of the element, with a Roman numeral indicating the ionization state of the emission line. For example, the emission lines of atomic iron are labeled Fe I and singly ionized iron Fe II. In addition to spectral lines, continuum radiation can be seen as background signal in the spectra. If the optical fiber had been directed at the melt, thermal radiation would also have been seen. However, these two contributions are very small compared to the high intensity of the spectral lines.

The emission lines of specific elements were identified from the spectra by comparing their wavelengths with the information of known emission line wavelengths from the National Institute of Standards and Technology (NIST) database.[32] An example spectrum is presented in Figure 3.

The intensity of the emission line was determined by comparing its height to the background intensity in its surroundings, which is why the intensity is in arbitrary units. The intensity of the emission line varies over time, not only because the presence of the corresponding element in the plasma varies, but also because the plasma arc moves around the crucible and is not always visible to the view cone of the optical fiber. Therefore, the intensities of the elements to be studied were normalized by the total intensity of the plasma. The normalized intensities were then used to plot the time series data.

The furnace atmosphere affects the propagation of light. When the atmosphere is optically thin, no significant absorption or reflection of radiation is observed. However, as the optical thickness increases, self-absorption may be observed.[33] Self-absorption occurs when an emitted photon is absorbed by another atom, usually of the same element, and again emitted in an arbitrary direction which may be different from the one to which the photon was initially directed. This decreases the intensity of radiation for that specific emission line, and since the decrease in intensity is strongest at the center of the emission line, the line broadens.[33] The broadening can be used to estimate the level of self-absorption in the spectra. If self-absorption is very strong, the emission line can also be self-reversed, which appears as a minimum in the middle of the emission peak. Several authors have suggested ways to correct self-absorption in spectra,[34–36] but correcting it is beyond the scope of this article. However, since Na I emission lines are very susceptible to self-absorption, the time points where self-absorption significantly affects the spectra were calculated. The effect of self-absorption was seen by comparing the total width of the two sodium D lines (588.99 and 589.59 nm) over time. In this way a limit for self-absorption was found, and the spectra in which the lines were wider than the limit were considered to be affected by self-absorption.

The temperature of the plasma can be calculated using the Boltzmann theory, in which the intensities of different emission lines pertaining to the same excited and decayed element are compared to each other.[37] As the plasma temperature increases, more atoms are excited to higher-energy states, so that consequently the intensity of those emission lines with respect to the ground state intensity correlates with the plasma temperature. The Boltzmann equation is

$$\ln\left(\frac{\epsilon^z \lambda_{mn}}{g_m A_{mn}}\right) = -\frac{1}{k_B T} E_m^z + \ln\left(\frac{hcN^z}{4\pi U^z(T)}\right), \qquad [2]$$

where ϵ is the wavelength-integrated emissivity, z is the ionization state, λ is the wavelength of the emission line, m and n are the upper and lower energy states respectively, g is the degeneracy of the energy state, A is the transition probability, k_B is the Boltzmann constant, T is the plasma temperature, E is the energy of an energy state, h is the Planck constant, c is the speed of light in vacuum, N is the number density, and $U(T)$ is the partition function. The second term on the right-hand side of Eq. 2 assumes a constant value. When the remaining right-hand side term is plotted with respect to the left-hand side of the equation for several emission lines of the same element, the plasma

Table II. Fe I Emission Lines Used in the Plasma Temperature Calculations

λ_{mn} (nm)	A_{mn} (s^{-1})	E_n (eV)	E_m (eV)	g_m
352.604	1.14×10^6	0.087	3.603	7
360.668	8.29×10^7	2.692	6.129	13
404.581	8.62×10^7	1.485	4.549	9
406.359	6.65×10^7	1.557	4.608	7
407.174	7.64×10^7	1.608	4.652	5

Table III. RGB Limits for the Recognition of Blue and Yellow Pixels in the Video Frames

RGB	Blue1	Blue2	Yellow
R_{min}	B/3	B/2.7	140
R_{max}	B/1.6	B/1.4	255
G_{min}	B/1.8	B/1.76	R/2.55
G_{max}	B/1.2	B/1.05	R/1.1
B_{min}	140	180	0
B_{max}	180	255	R/1.4
$(R/G)_{max}$	—	1.1	0.86

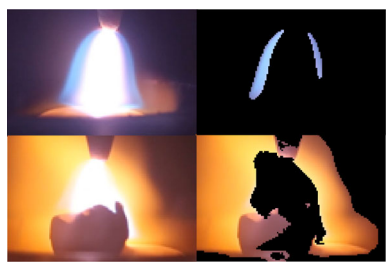

Fig. 4—Original (top left corner) and blue-masked frame (top right corner), and original (bottom left corner) and yellow-masked frame (bottom right corner) (Color figure online).

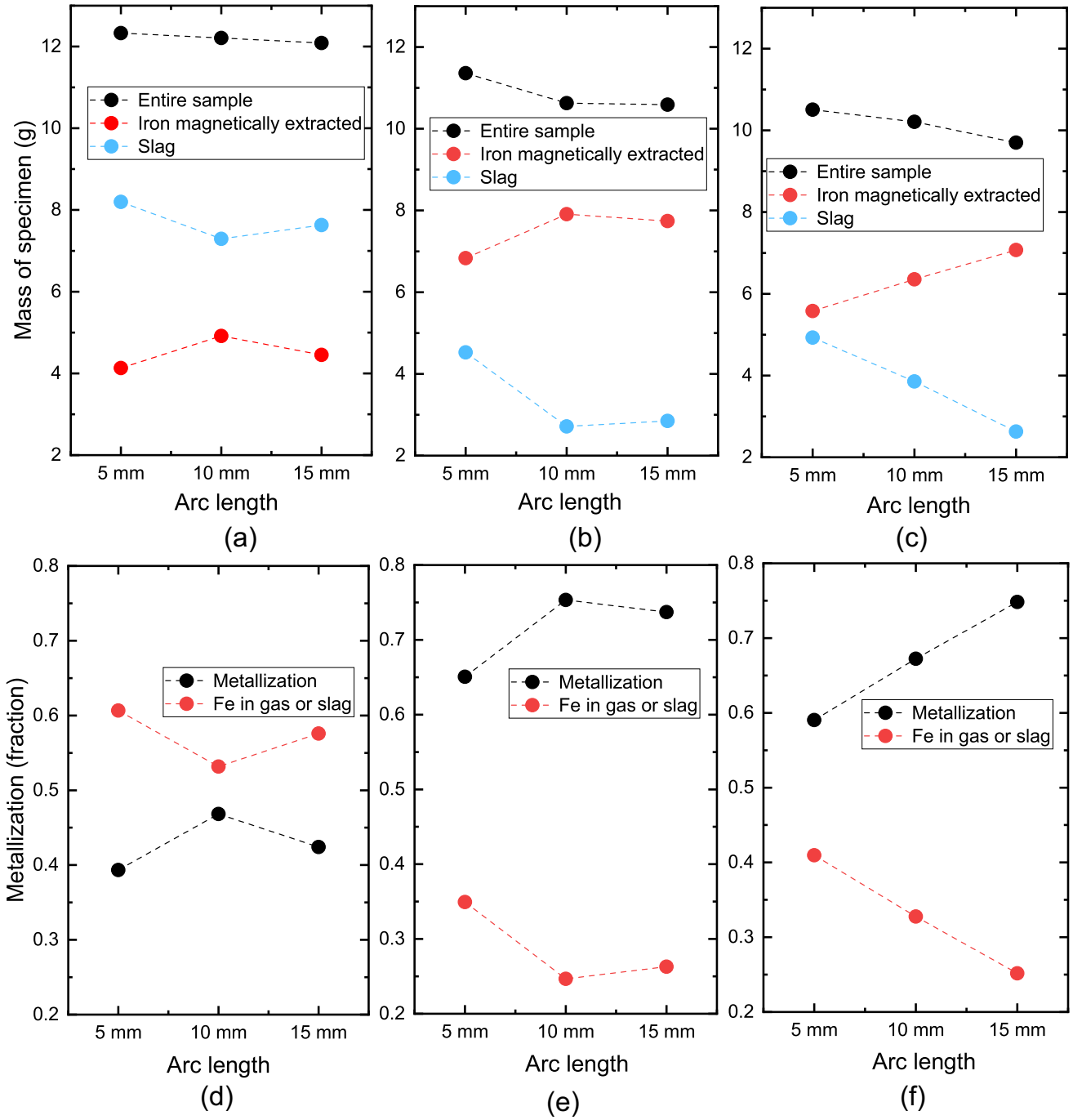

Fig. 5—Sample masses after reduction as a function of arc length at the current of (*a*) $I = 100$ A pure hematite, (*b*) $I = 200$ A pure hematite, and (*c*) $I = 200$ A fluxed hematite experiments. Degrees of metallization as a function of arc length at the current of (*d*) $I = 100$ A pure hematite, (*e*) $I = 200$ A pure hematite, and (*f*) $I = 200$ A fluxed hematite experiments.

temperature can be calculated from the slope of the plot. Fe I emission lines presented in Table II were used to calculate the plasma temperature.

The electron density was calculated from the broadening of the hydrogen beta line ($\lambda = 486.135$ nm) using the model suggested by Surmick and Parigger.[38] The model is based on Stark broadening of the hydrogen lines and can be written as

$$N_e = 10^{17} \cdot \left(\frac{\Delta w_{H_\beta}}{4.50} \right)^{1/0.71}. \quad [3]$$

In Eq. [3], Δw_{H_β} is the FWHM of the hydrogen beta line, which was calculated by fitting a Lorentzian to the hydrogen beta emission lines in the spectra.

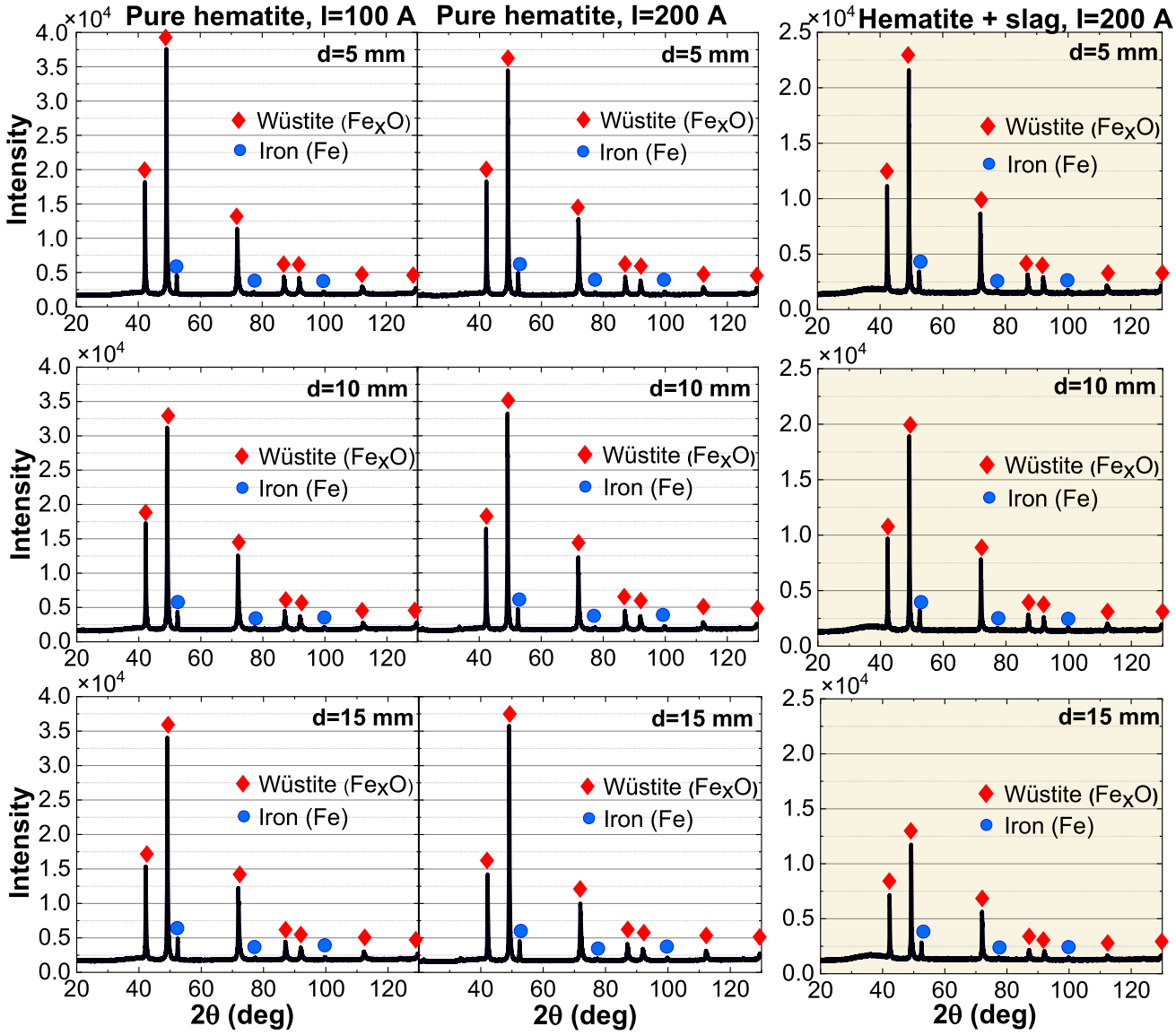

Fig. 6—The XRD results of the slag composition. Left column: pure hematite experiments with the current $I = 100$ A and arc length d, middle column: pure hematite experiments with the current $I = 200$ A, right column: fluxed hematite experiments. Note that the fluxed hematite experiments have a lower maximum value of the y-axis compared to the pure hematite experiments.

C. *Image Analysis*

To be able to compare the video frames with the corresponding spectra, their timestamps needed to be synced. Since the video frames did not have any time information, artificial time stamps were assigned starting from the ignition to the extinction of the electric arc to better correspond the spectra to the video frames. For each spectrum, the frame corresponding to the closest video timestamp was used in the image analysis.

To investigate the relationship between the colors of the video frames and the spectra, blue and yellow pixels were first identified from the frames. This was done by defining the RGB values for those pixels that subjectively looked like the color in question and masking the frames by them. The RGB values were adjusted by comparing at least ten different frames for each color to account for all possible shades of the color. The final RGB value limits for blue and yellow are presented in Table III.

For example, the B values for blue are defined as numbers, whereas R and G are defined with respect to B. Note that for blue there are two different criteria: one where B is between 140 and 180 (Blue1) and one where B is larger than 180 (Blue2) to account for low- and high-intensity images, respectively. If the pixel matched one of those criteria, it was considered a blue pixel. An example of the original and masked images is presented in Figure 4.

Finally, the number of blue and yellow pixels in each frame was calculated and compared to the intensities of the respective emission lines.

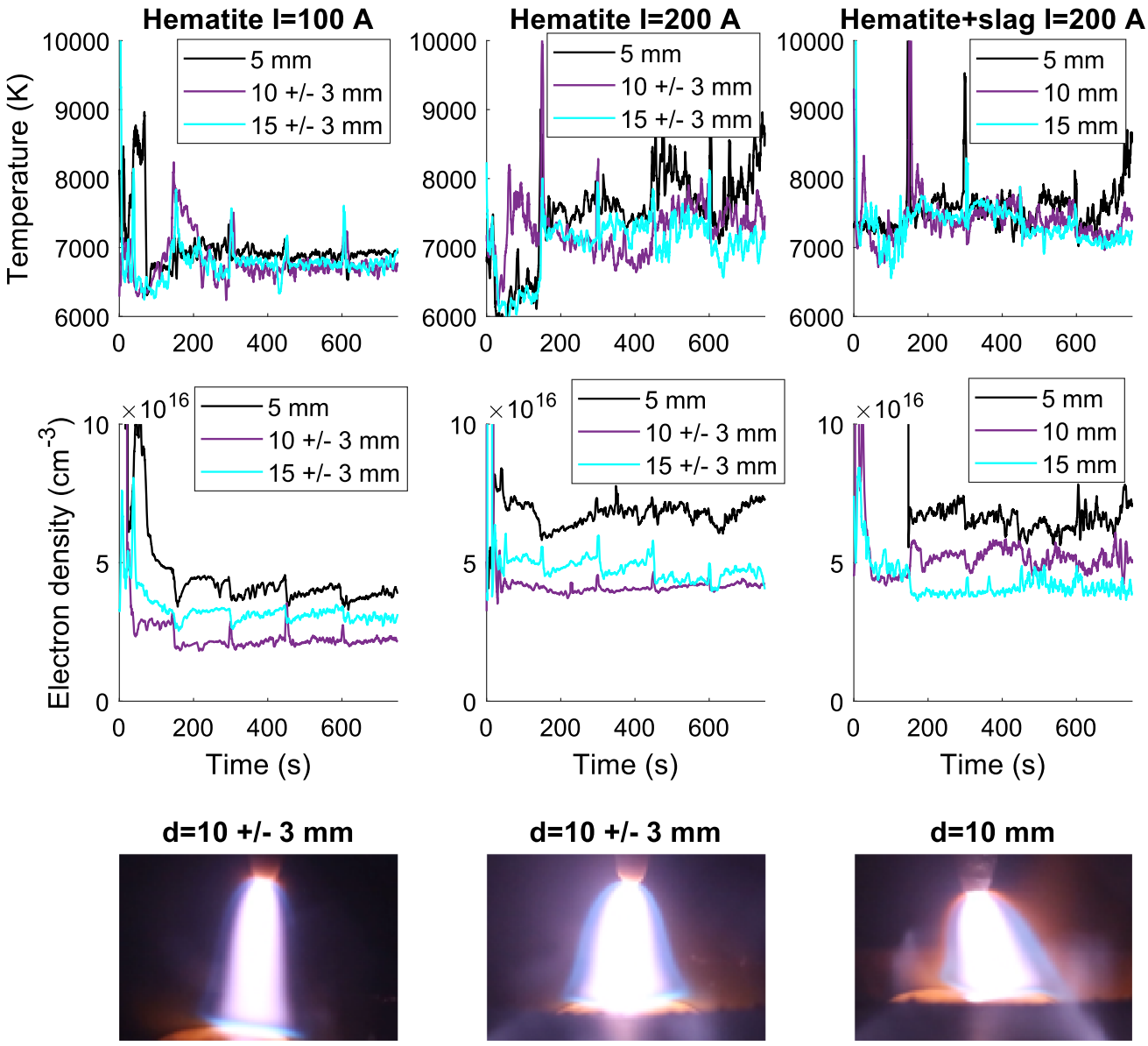

Fig. 7—Plasma temperatures (top panel) and electron densities (middle panel) as a function of time. Left column: pure hematite with current $I = 100$ A, middle column: pure hematite with the current $I = 200$ A, right column: fluxed hematite. The arc lengths d are presented in colors defined in the legend. In the bottom panel, images of the plasma in respective $d = 10$ mm arc length experiments are shown (Color figure online).

III. RESULTS AND DISCUSSION

A. *Final Chemical Compositions of the Samples*

The masses of the samples after reduction are presented in Figures 5(a) through (c) and their metallization degrees in Figures 5(d) through (f).

The iron was extracted by crushing the sample and magnetically separating the iron from the slag, after which the degree of metallization was calculated by dividing the total mass of the reduced Fe by the total amount of Fe available in the original input hematite. The small amounts of metallic iron trapped in the slag phase were included in the degree of metallization. For the current $I = 100$ A (Figure 5(a)), the total masses of the samples are the highest, so the amount of material lost by evaporation is the smallest. The mass of the entire sample in the fluxed experiments (Figure 5(c)) is the lowest, with the mass of the slag approximately the same magnitude as in the pure hematite $I = 200$ A experiments (Figure 5(b)). Therefore, the addition of the slag components seems to increase the evaporation of the metal. For the pure hematite experiments with $I = 100$ A, the iron mass is much lower than for $I = 200$ A. Combined with the previous note of a lower level of evaporation, a significant amount of iron must have been lost to the slag as iron oxide. The same can be seen from the degree of metallization, which is significantly lower in the $I = 100$ A experiments

(Figure 5(d)), and the amount of iron in the gas or slag state, respectively, higher than for the $I = 200$ A experiments (Figures 5(e) and (f)). Therefore, the current of 100 A is too small to effectively reduce hematite to iron under these conditions. It is also interesting that for $I = 100$ A and $d = 10$ mm, the degree of metallization is higher than for the respective $d = 15$ mm experiment, while in the $I = 200$ A pure hematite experiments the degree of metallization plateaus, and in the fluxed hematite experiments it increases with the arc length. The reason for this may be the small inaccuracies in the arc length, which are further discussed in Section III–B.

The highest degree of metallization and the lowest amount of iron lost in the slag or in the evaporation state is achieved with pure hematite when using $I = 200$ A and $d = 10$ mm. For the fluxed hematite experiments, the degree of metallization increases linearly with the arc length, suggesting that a longer arc in conjunction with a larger contact area with the molten pool appears to favor the reduction.

The results of the slag phase XRD analysis are presented in Figure 6.

The results show that the slag contains two phases, wüstite and metallic iron. Therefore, it can be assumed that the unreduced iron oxide concentrated in the slag is mainly wüstite. Since SiO_2, CaO and Al_2O_3 are good glass formers especially in conjunction with high cooling rates, in the fluxed hematite experiments they seem to concentrate in a glassy phase formed in the interdendritic zones of the slag as indicated by the diffused humps between $2\theta = 30 - 40$ in the XRD plots. The intensities of both wüstite and metallic iron are smaller in the fluxed hematite experiments compared to the pure hematite experiments. Between the pure hematite experiments, the differences in intensity are so small that no conclusions on the effect of current or arc length can be drawn.

Table IV. Time-Averaged Voltage Values in the Experiments

Experiment	Voltage (V)
1	29.8
2	26.9
3	23.2
4	22.3
5	26.1
6	25.7
7	21.4
8	24.2
9	26.7

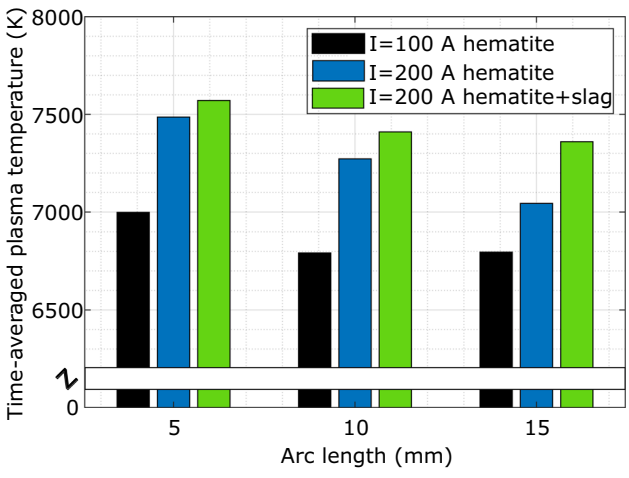

Fig. 8—Time-averaged plasma temperatures for different currents I, arc lengths d and sample materials.

B. *Spectral Analysis*

In the following time-series figures, the data have been averaged over five seconds. All emission line intensities have been normalized by the total intensity of the plasma to take into account the visibility of the arc to the optical fiber. Spectra for the fluxed hematite experiment with $d = 5$ mm (Exp 7) are available from $t = 150$ seconds onward due to a failure in the OES recording in the initial stages of the experiment.

In Figure 7, the Fe plasma temperatures (top panel) and the electron densities (middle panel) are presented as a function of time.

The start of all 2.5 minutes steps can clearly be seen as a higher temperature fluctuation. Some differences in the level of the Fe plasma temperatures between experiments with different currents and input materials can be seen. This is also visible in Figure 8, where the time-averaged Fe plasma temperatures of all the experiments are presented for different arc lengths.

The average plasma temperatures are significantly higher for the $I = 200$ A experiments than for the $I = 100$ A experiments, which can be expected due to the higher energy input. The fluxed hematite experiments also exhibit slightly higher plasma temperatures compared to the pure hematite experiments, which may be one reason for the higher evaporation of iron observed in Figure 5.[18] In all experiments, the average plasma temperature decreases with the increasing arc length, which is due to the decreasing energy density.

Using the measured temperature range, it is possible to estimate the chemical composition of the plasma computationally. To this end, the equilibrium composition was calculated as a function of temperature using FactSage ver. 8.3. The calculations were performed using the FactPS database (including gaseous ions) and treating the gas phase as a real gas. Figure 9 shows the calculated equilibrium composition of 10 vol pct H_2 + 90 vol pct Ar gas mixture from 1000 to 11,000 K under a pressure of 1 atm. It is seen that under the temperatures relevant for this work, hydrogen is present mostly as atomic H. In this regard, possible differences in the gas phase compositions are unlikely to explain the experimental results obtained.

Figure 7 shows that the electron densities for $I = 200$ A are higher than for $I = 100$ A, which is caused by a higher level of ionization. The electron density seems to fluctuate more in the fluxed hematite experiments. The evaporation of ions is complicated by the presence of slag components, and since electrons recombine with evaporated ions, the electron density

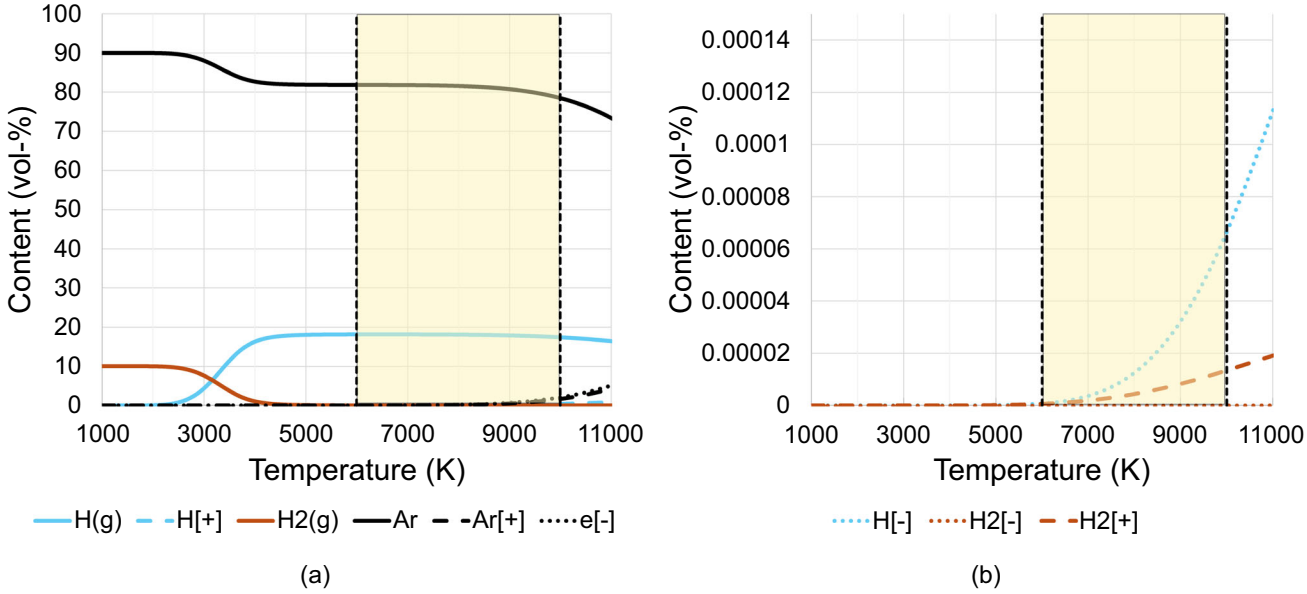

Fig. 9—The estimated chemical composition of the plasma as a function of temperature, where (*a*) shows the major components and (*b*) shows the minor components. The shaded area represents the region of the Fe temperatures in this study.

fluctuates with the number of ions in the plasma. In fluxed hematite experiments according to the spectra, those ions include mostly Fe and Ca.

The electron density is defined as the number of electrons per unit of volume. With a longer arc, electrons are distributed into a larger volume, which decreases their density. However, since the electrode was manually moved during the experiments, the distance between the electrode tip and the sample was not constant: the electron densities for the $d = 10$ mm pure hematite experiments are lower than their respective electron densities with $d = 15$ mm. In Figure 7, the images below the plots show the plasma arcs in all the $d = 10$ mm experiments. In pure hematite experiments (left and middle) the arc seems longer than in the fluxed hematite experiment (right). Furthermore, the length of the arc affects the voltage, because a longer arc requires a higher voltage to ignite and remain stable. The median voltage values presented in Table IV show that the voltages are the highest for experiments 1 and 2 ($d = 10$ mm) and the lowest for experiments 3, 4 and 7 ($d = 5$ mm). For the reasons presented above, a variation range of $\pm$ 3 mm was added to the headings of the $d = 10$ mm and $d = 15$ mm pure hematite experiments. In all $d = 5$ mm experiments and experiments with fluxed hematite, the electron densities and voltages seem to be consistent with respect to each other, so no variation range was added to these plots. This suggests that the electron density could possibly be used as an estimate for the arc length if the arc cannot be visually monitored, for example in industrial-scale reactors.

Figure 10 represents the relative intensities of the atomic iron emission lines (Fe I, $\lambda = 440.475$ nm, upper panel) and ionized iron emission lines (Fe II, $\lambda = 266.466$ nm, lower panel).

As the figure shows, the emissions are strong at the start of the experiment because as the arc is ignited and the sample starts to melt, some sample material evaporates. Toward the end of the $I = 100$ A experiments, the Fe I intensity tends to increase. However, for the $I = 200$ A pure hematite experiments, the intensity does not change significantly over time. For the lower current experiments, the rate of ionization is lower than in the higher current experiments due to the lower temperature and energy density. This is in line with Figure 10, where Fe I emissions are stronger and Fe II emissions weaker for the $I = 100$ A experiments compared to the $I = 200$ A experiments. The higher electron density for the $I = 200$ A experiments shown in Figure 7 also indicates a generally higher level of ionization compared to the $I = 100$ A experiments. The ionizing effect of a higher energy input should be seen for other elements as well.

For fluxed hematite experiments, strong Fe I fluctuations can be seen. With respect to the small sample size, turbulent flows in the melt caused by the plasma are very strong. The slag components move around the melt with the flow and simultaneously complicate the evaporation kinetics of iron. When the slag components are floating on top of the melt, they insulate the contact between the plasma and the molten oxides to some extent, so that a smaller amount of oxides is reduced and less iron is evaporated. On the other hand, if the slag components are submerged and the arc hits an oxide-rich part of the melt, oxides are reduced and some iron evaporates. This can explain the oscillating behavior of Fe I observed in the fluxed hematite experiments. The effect that enhances evaporation, however, seems to be stronger than the insulating effect of the slag components, based on the smaller final mass of the metal phase in the fluxed hematite experiments shown in Figure 5. When the slag components floating on the top of the melt are suddenly

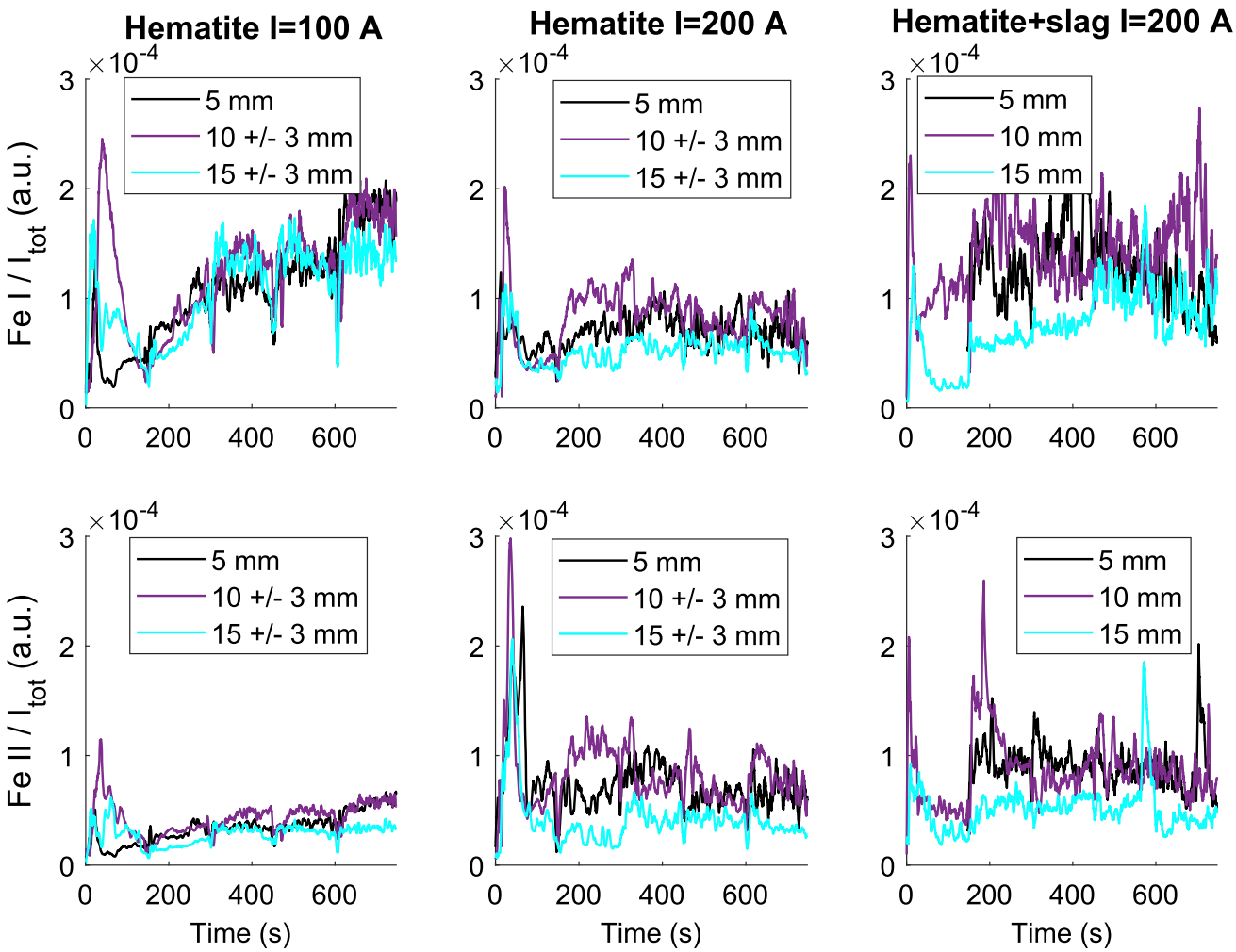

Fig. 10—Intensities of the atomic iron emission line (Fe I, top panel) and the singly ionized iron emission line (Fe II, bottom panel) with respect to the total intensity of the spectrum I_{tot}. Left column: pure hematite with current $I = 100$ A, middle column: pure hematite with current $I = 200$ A, right column: fluxed hematite. The arc lengths d are presented in colors defined in the legend (Color figure online).

submerged by the turbulent flow, the sudden exposure of iron oxides to plasma may vaporize iron more strongly than the constant exposure in the pure hematite experiments, increasing the amount of Fe lost to evaporation.

Figure 11 represents the time evolution of the slag components, *i.e.*, ionized calcium (Ca II, $\lambda = 396.847$ nm, upper panel), atomic silicon (Si I, $\lambda = 288.158$ nm, middle panel) and atomic aluminum (Al I, $\lambda = 396.152$ nm, lower panel).

The limits of the y-axis are the same for all Ca II plots, but for the Si I and Al I lines, the limits for pure hematite experiments are an order of magnitude smaller than those in the fluxed hematite experiments due to the very small amount of silicon and aluminum oxides present in the pure hematite. Consequently, the Si I and Al I intensities, as well as the Ca II intensities, are significantly stronger in the fluxed hematite trials compared to the pure hematite experiments. The fluctuations of the elements presented in the figure increase toward the end of the fluxed hematite experiments, where a slag layer is formed. Once the arc hits the slag, some slag evaporates, producing strong emissions of the slag components. Therefore, a similar effect described for iron evaporation also affects the slag components. In the fluxed hematite experiments, the longer arc ($d = 15$ mm) seems to make the fluctuations smaller, especially during the first 450 seconds of the experiment. This applies to both the Fe and the slag component emissions. The phenomenon may be caused by a broader contact area between the plasma and the melt, allowing for a more constant interaction between the sample components and the plasma, and avoiding sudden increases in evaporation. In the $I = 200$ A pure hematite experiments, a similar effect can be seen, while in the $I = 100$ A experiments the arc length does not affect the emissions very much.

Like the Fe I intensities in Figure 10, the intensities in Figure 11 $I = 200$ A experiments are also decreased by ionization. This can be seen especially in the emissions of Ca II, which can be further ionized to Ca III, but also in the intensities of Si I and Al I. Another reason for the decreasing Ca II intensities can be self-absorption. Like atomic sodium, singly-ionized calcium is also susceptible

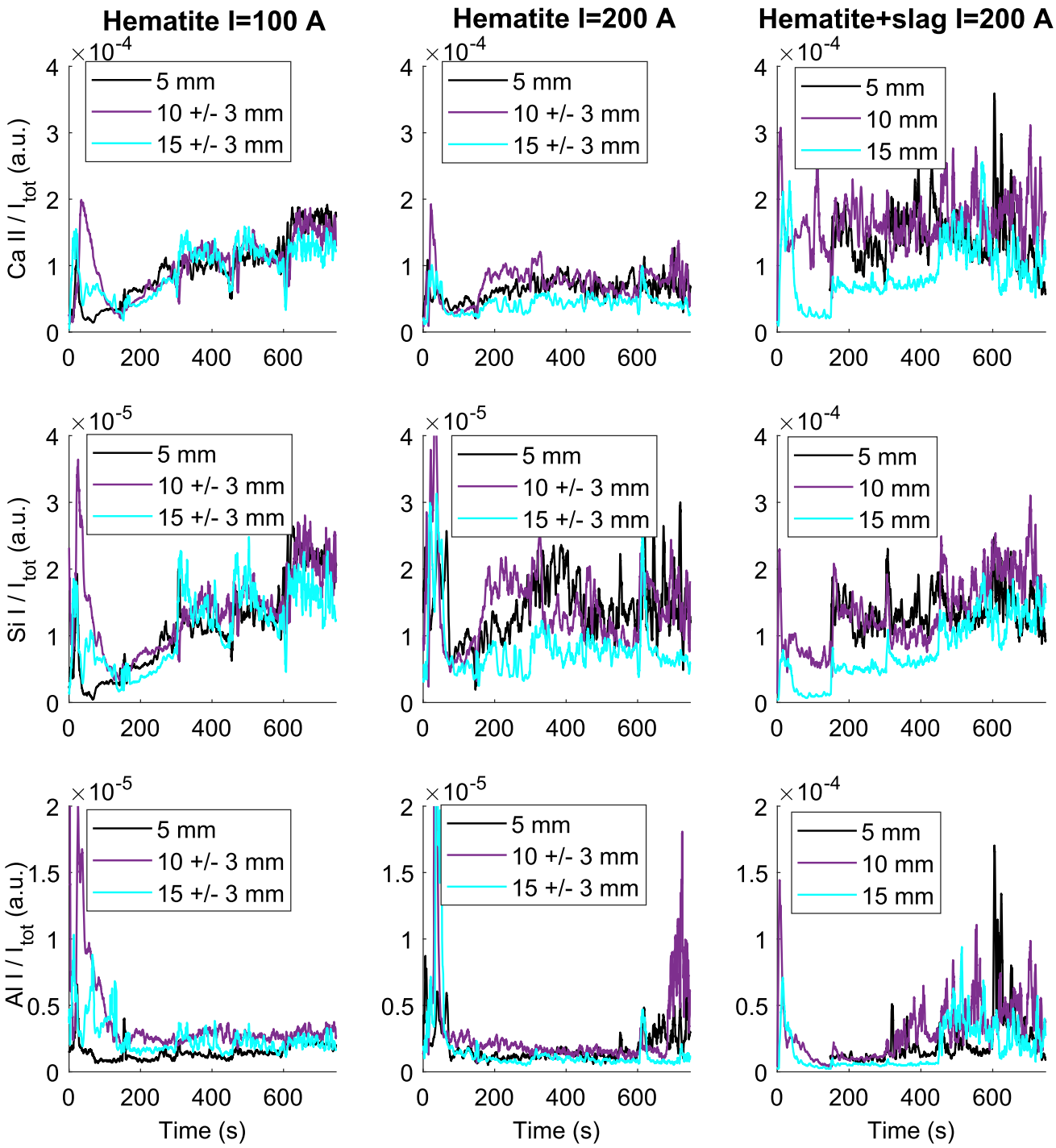

Fig. 11—Intensities of the singly ionized calcium emission line (Ca II, top panel), the atomic silicon emission line (Si I, middle panel) and the atomic aluminum emission line (Al I, bottom panel) with respect to the total intensity of the spectrum I_{tot}. Left column: pure hematite with current $I = 100$ A, middle column: pure hematite with current $I = 200$ A, right column: fluxed hematite. The arc lengths d are presented in colors defined in the legend (Color figure online).

to self-absorption, which reduces the intensity of the spectral lines. At high currents, the rate of ionization is high, as indicated by the high electron density in Figure 7 $I = 200$ A experiments. This refers to a high number density of ionized species, such as Ca II. Thus, the medium is optically thick for ionized species, resulting in higher self-absorption and lower emission line intensities compared to lower currents. If OES is used in industrial-scale furnaces to monitor the slag formation, self-absorption should be taken into account, for example by monitoring other Ca II emission lines that have smaller inherent intensities.

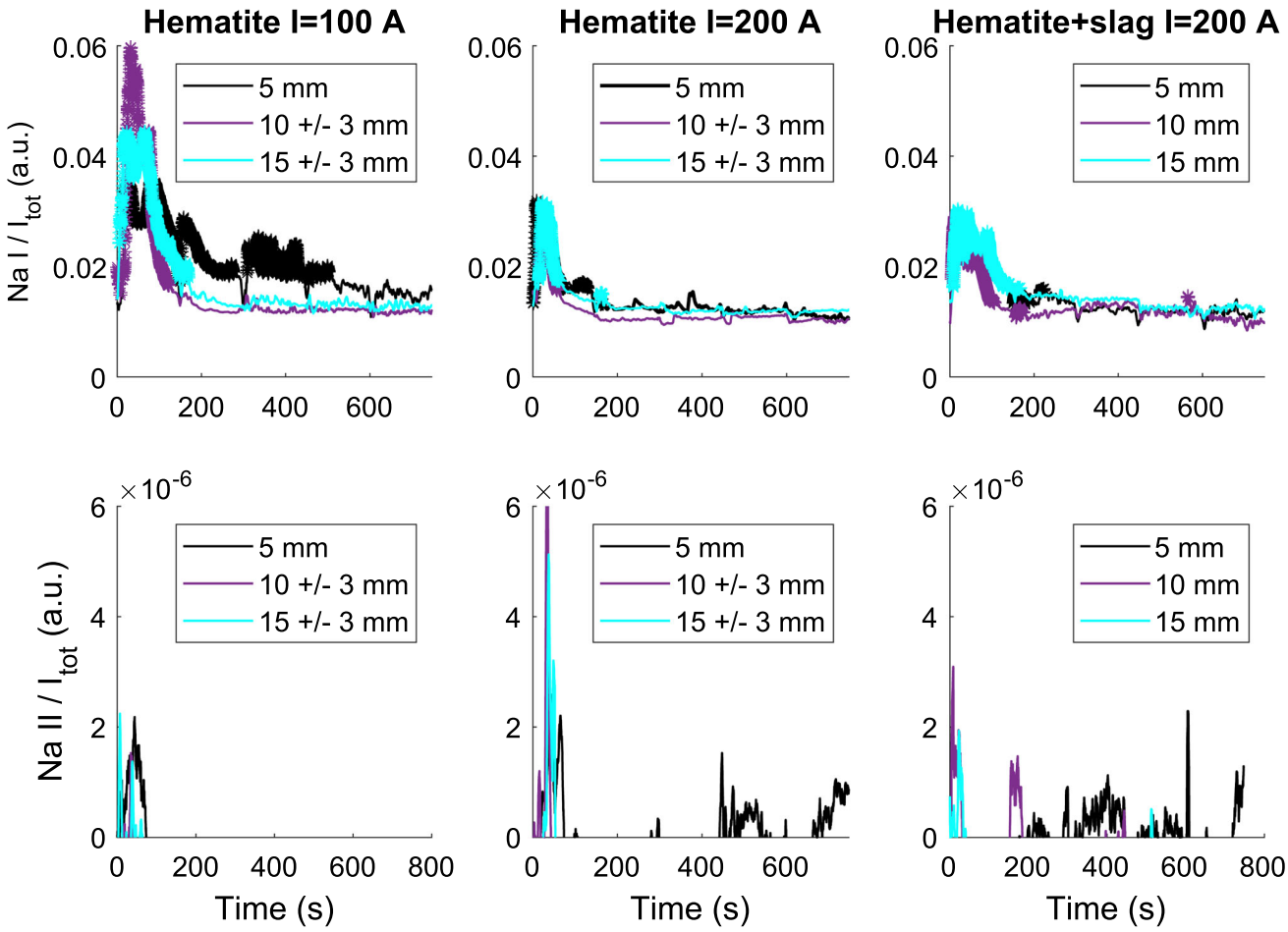

Fig. 12—Intensities of the atomic sodium emission line (Na I, top panel) and singly ionized sodium emission line (Na II, bottom panel) with respect to the total intensity of the spectrum I_{tot}. Left column: pure hematite with current $I = 100$ A, middle column: pure hematite with current $I = 200$ A, right column: fluxed hematite. The arc lengths d are presented in colors defined in the legend. In the Na I plots, the time points where self-absorption affects the spectra have been marked with asterisks (Color figure online).

Sodium is not a significant component in iron ores: for example Das *et al.*[39] found that their hematite contained as little as 0.0929 pct sodium. However, since sodium emission line intensities are usually very strong, they can easily be distinguished from or even dominate the OES spectra, even if the amount of sodium in the ore is negligible. In Figure 12, the time evolution of atomic sodium (Na I, summed intensity around emission lines $\lambda = 588.995$ nm and $\lambda = 589.592$ nm, upper panel) and singly ionized sodium (Na II, $\lambda = 459.093$ nm, lower panel) is presented. The time points where self-absorption or even self-reversal significantly affects the Na I emission lines are marked in the plots by asterisks.

The strongest sodium emissions occur at the beginning of each experiment, as sodium is evaporated from the melt. This can also be seen in the videos as a strong yellow/orange glow around the plasma. In all experiments, the sodium intensity decreases over time, which is in line with the results of Das *et al.*[39] Arc length does not significantly affect the intensity of the sodium emissions. Like the other elements described earlier, sodium is also ionized more strongly in the experiments with $I = 200$ A, which is shown as a decrease in the Na I intensities compared to the experiments with $I = 100$ A. The level of Na II emissions is overall very low, but especially for $d = 10$ mm, $d = 15$ mm and $I = 200$ A, sodium ionizes strongly at the beginning of the experiment both for the pure and fluxed hematite cases, a

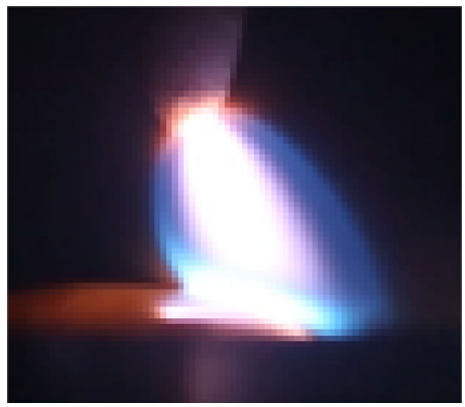

Fig. 13—An example of the yellow glow around the electrode in experiment 3.

finding which supports the hypothesis. However, the time evolution of the sodium emission lines should be further investigated in future studies to shed light on the behavior of alkali emissions over the course of the reduction process.

The Na I intensity of the experiment 3 with $I = 100$ A and $d = 5$ mm shows a slightly different behavior from the other experiments with $I = 100$ A. The intensity decreases less as a function of time than in the other experiments, and it seems to be more influenced by self-absorption. In the videos, a yellow glow around the electrode can be seen throughout the experiment, which may be the source of the strong Na I emissions. An example of the glow is shown in Figure 13.

If the optical fiber was pointed at the tip of the electrode, it would have seen mainly the yellow glow, which could explain the large Na I emissions observed in this experiment. This could possibly be mitigated in future laboratory-scale studies by using a lens system that allows for a broader field of view.

C. *Image Analysis*

Standardized Fe I emission line intensities ($\lambda = 440.475$ nm) and standardized number of blue pixels in the corresponding video frames are presented as a function of time in Figure 14. The Fe I emissions are represented by continuous lines, and the number of pixels of the corresponding experiment are shown on top of them by dashed lines.

Overall, there are similar trends in the emissions and the pixels: for example, after 600 seconds in the pure hematite experiment with the current $I = 200$ A and the arc length $d = 15$ mm, an increase is observed in both the Fe I intensity and the number of blue pixels. The number of pixels also tends to fluctuate more with fluctuating emissions. However, during the first 30 seconds of the experiments the emissions are strong, but the number of blue pixels does not follow them. As the sample is being melted, some sample material evaporates, and electromagnetic radiation is emitted by many elements, creating a mix of colors observed around the plasma. Therefore, even if the optical emissions are strong, the blue color cannot be observed as clearly as later on in the experiments, which results in a very small number of blue pixels detected. In Figure 15, a comparison of the spectra and the number of pixels to the simultaneous images of the plasma is presented. The lack of blue pixels in the initial stages of the experiment can be seen in Figures 15(a1) through (a3).

After the melting, the emissions and the number of blue pixels are low for approximately 150 to 300 seconds, indicating the ongoing reduction of iron oxide (Figures 15(b1) through (b3)). Once some iron is reduced, the emissions and the number of blue pixels start to fluctuate, and the blue pixels are more clearly visible in the images (Figures 15(c1) through (c3)).

Figure 14 shows that in the pure hematite experiments, the number of blue pixels reacts to changes in the Fe I intensities similarly for all arc lengths and currents used. However, the addition of the slag components affects the balance between the pixels and the emissions. For example, in the $d = 10$ mm fluxed hematite experiment after $t = 150$ seconds, the emissions fluctuate a lot more than the number of pixels. The optical emissions from the slag components can change the wavelength distribution of the light emitted by the plasma, and therefore the hue of the blue color in the images. However, Figures 15(d1) through (d3) shows that the blue pixels are quite well identified from the image. Consequently, the reason for this mismatch between Fe I emissions and the number of blue pixels must be that the high fluctuation of the emissions cannot be seen as a high fluctuation of the number of pixels.

A time series for the summed Na I intensities (around $\lambda = 588.995$ nm and $\lambda = 589.592$ nm) and the number of yellow pixels is presented in Figure 16.

The relation between the emission line intensities and the pixels at the beginning of the experiments is better than for the Fe I emissions and the blue pixels, perhaps due to the high evaporation of Na during melting. As seen also in the lower part of Figure 4, the entire atmosphere glows yellow during the melting, so the

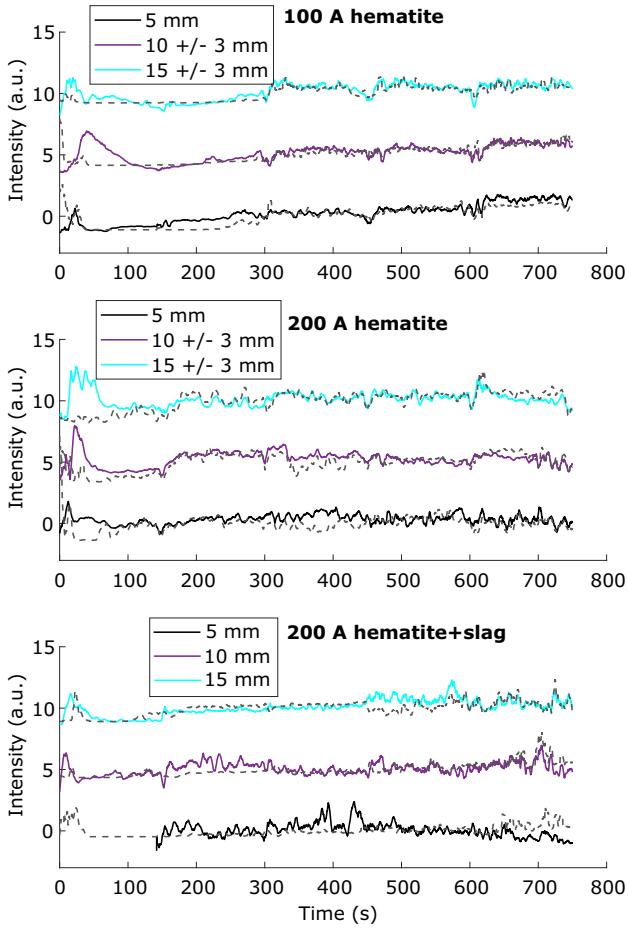

Fig. 14—Standardized 5 seconds averaged time series of Fe I emissions (continuous lines) and the standardized number of blue pixels (dashed lines) in pure hematite experiments with current $I = 100$ A (top), pure hematite experiments with current $I = 200$ A (middle) and fluxed hematite experiments (bottom). The arc lengths d are presented in colors defined in the legend. An offset of 5 and 10 a.u. was added to $d = 10$ and 15 mm experiments, respectively, to show the curves more clearly (Color figure online).

yellow color can be easily identified from the video frames. The experiment with $I = 100$ A and $d = 10$ mm (Exp 1) makes an exception: the number of pixels decreases around 37 seconds, while the emissions do not. The video frames confirm the diminishing of the yellow color (Figures 15(e1) through (e3)). The strong emissions could be explained by the optical fiber being directed at the edge of the plasma, where the Na I emissions are the strongest. This shows how large a difference the positioning of the optical fiber and, on the other hand, the place where the sample is melted makes in small-scale experiments.

Figure 17 compares the plasma images with the Fe I plasma temperature at some significant points in the reduction process.

The plasma is unstable at the beginning of the experiment when the sample is melting (i). Shortly after the melting, the plasma behavior stabilizes, and simultaneously the plasma temperature is decreased by a few hundred degrees (ii). A slight decrease in the plasma temperature is also observed with the appearance of blue flashes in the video frames, which indicates a high degree of metallization (iii). At the end of the process (iv), no significant changes in the plasma temperature

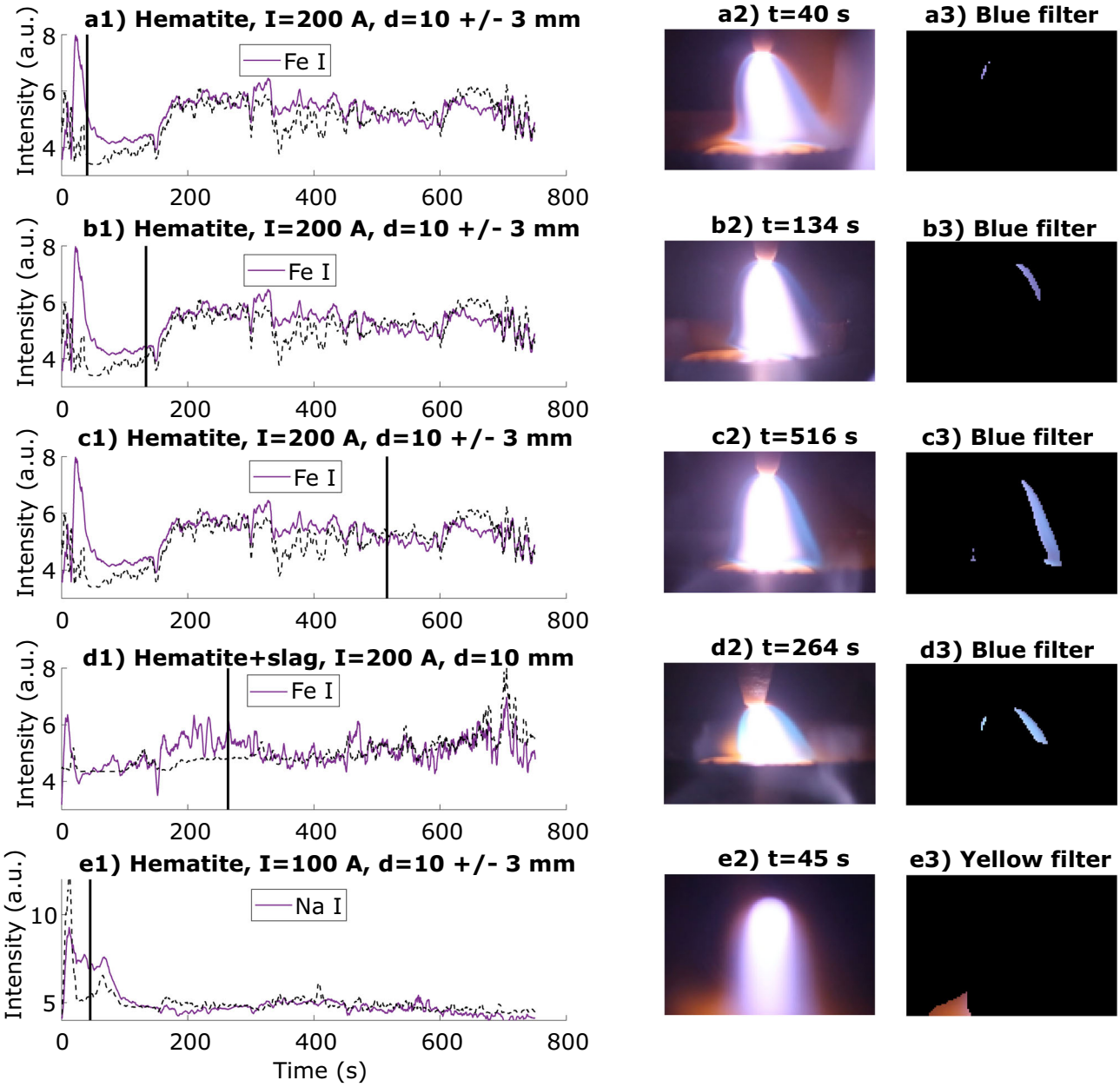

Fig. 15—Comparison of the OES time series and the number of pixels with the simultaneous images of the plasma. On the left column, a standardized time series of the Fe I or Na I emissions is presented by a continuous line and the number of blue or yellow pixels by a dashed line. The time points t shown in the middle and right column images on the same row are marked on the left column plots with a vertical line. The middle column shows the image of the plasma, and the right column shows the respective blue or yellow filter (Color figure online).

can be seen. Changes in plasma temperature may provide some information regarding the status of the reduction and the stability of the plasma.

D. *Application of OES in Industrial-Scale HPSR Furnaces*

Although the focus of this study is on laboratory-scale experiments, some notes on the industrial applications of OES are presented. Rautionaho *et al.*[40] list some possible problems with the detection of light by the OES method. For example, dust, fumes, foaming slag or reflections can hinder the reliability of the OES measurements. In industrial-scale furnaces, the movement of the arc on the molten bath can be erratic, so the location and direction of the measurement head should be carefully considered, allowing the best possible view cone for the arc.[27] However, due to the fiber being relatively far away from the plasma in industrial-scale furnaces, the view cone is naturally quite large, so the risk that the fiber does not receive any light is smaller than in laboratory-scale furnaces. The measurement head should also be protected from the extensive heat and possible slag splashes, for example by pressurized airflow as in the study by Pauna *et al.*[27] In industrial-scale facilities, optical fibers should also be well protected to prevent fractures or bending.

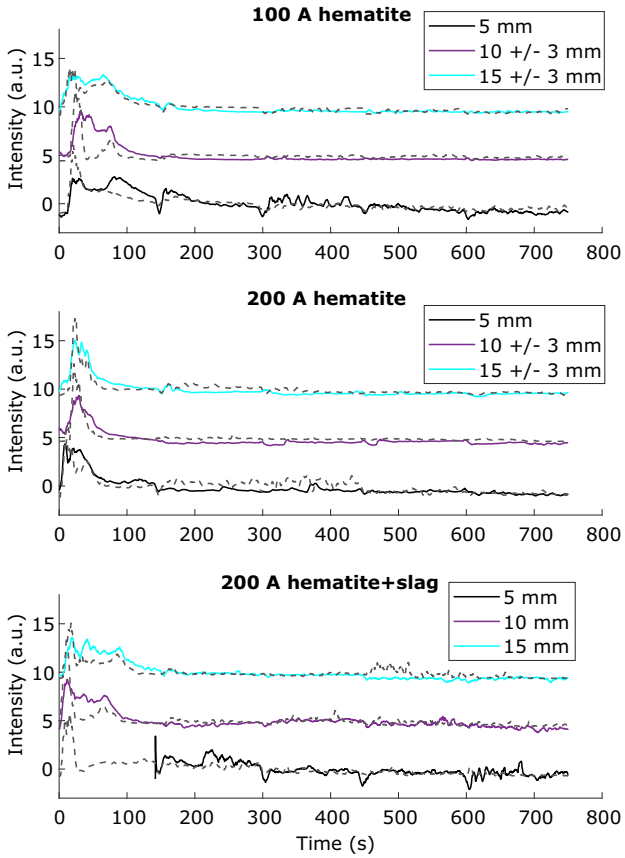

Fig. 16—Standardized 5 seconds averaged time series of Na I intensities (continuous lines) and the standardized number of yellow pixels (dashed lines) in pure hematite experiments with current $I = 100$ A (top), pure hematite experiments with current $I = 200$ A (middle) and fluxed hematite experiments (bottom). The arc lengths d are presented in colors defined in the legend. An offset of 5 and 10 a.u. was added to $d = 10$ and 15 mm experiments, respectively, to show the curves more clearly (Color figure online).

In electric arc furnaces, high temperature can corrode the refractory material if the arc power is too high,[41] which, due to the similarities between EAF and HPSR furnaces, could also be possible in the HPSR process. In that case, the plasma temperature should be well-controlled during the operation of the furnace, and OES could possibly be used as an online temperature measurement tool for this. Furthermore, it should be noted that other factors, such as slag acidity, also affect refractory wear[20] and may be even more relevant than high temperatures for industrial-scale furnaces. However, erosion of the refractory material and the factors affecting it should be further studied in HPSR furnaces to confirm the effect.

OES has many benefits as a process monitoring method. Since OES can be used continuously to monitor the reduction mechanisms under plasma exposure, the process does not need to be slowed down or stopped for sampling, which saves time and is economically more feasible due to shorter process times. Compared with sampling, OES may also give a more extensive view of the composition of the melt, not only because the measurements are continuous but also because they cover the entire molten surface and the plasma. OES has been commercialized for EAFs with the reported benefits of 3 to 8 pct savings in power consumption and 5 to 8 pct increase in production,[42] which is promising for developing a similar method for the HPSR process.

IV. CONCLUSIONS

In continuation of earlier studies, this study provides detailed information on the analysis of HPSR spectra and plasma images during the reduction of hematite. The results indicate that with the higher current ($I = 200$ A), the degree of metallization and the evaporation of the samples were higher than with the lower current ($I = 100$ A). The effect of the arc length on the degree of metallization was found to be nonlinear, perhaps because of small inaccuracies in the arc length. The XRD results showed that the slag is composed of wüstite and metallic iron, and possibly a glassy amorphous phase in the fluxed hematite experiments due to the high cooling rate caused by the use of a Cu crucible.

The plasma temperature increased with the current, and it was higher for fluxed hematite than for pure hematite. The increasing arc length was found to decrease the average plasma temperature. Furthermore, increasing the arc length decreased the electron density as a result of increasing plasma volume, although the effect was inconsistent for some experiments. Because there were possibly some small inaccuracies in the arc length, determining the electron density was found to be a potential method to monitor it. When comparing the emission line intensities of individual species, the neutral line intensities were found to be higher with a lower current due to a lower level of ionization. The varying contact between the plasma and the iron oxides

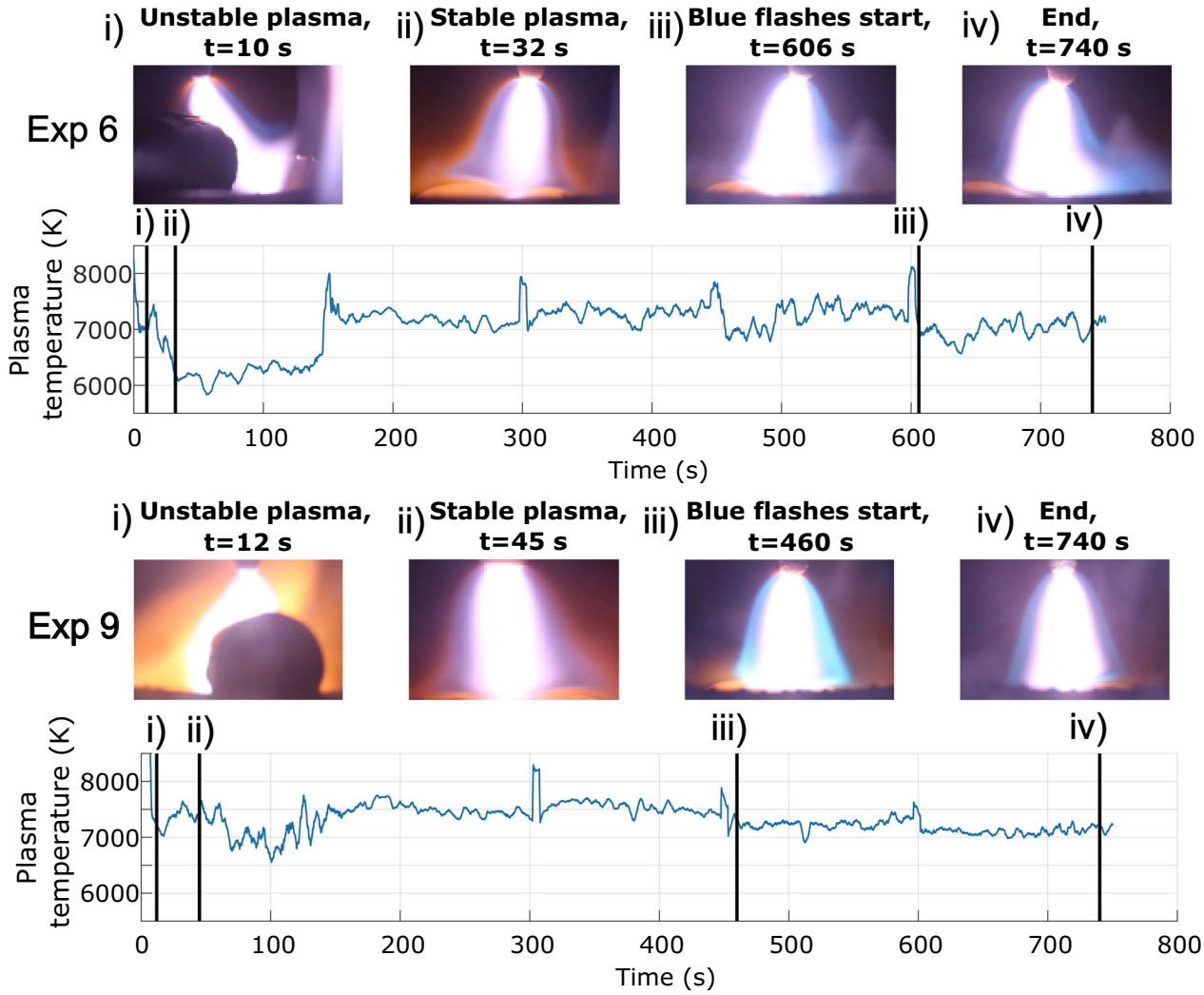

Fig. 17—Plasma images at (*i*) unstable plasma, (*ii*) stable plasma, (*iii*) the start of the blue flashes and (*iv*) the end, and the Fe I plasma temperatures in experiments 6 and 9. The time points representing (i) through (iv) are shown in the plasma temperature plots by vertical lines.

increased the evaporation of Fe in slag-fluxed experiments. However, with a longer arc, the contact area was more stable, which decreased the Fe OES intensities. The emission lines of the slag-related species (Ca II, Si I, and Al I) were found to be distinct in the slag-fluxed experiments.

Even if the Fe I emission line intensities and the number of blue pixels were found to follow the same patterns, no clear linear correlation was found between them nor between the Na I intensities and the number of yellow pixels. One factor affecting this is the change of the hue of the plasma with the evaporation of different elements, which makes color recognition difficult, especially during and right after melting. The positioning of the optical fiber or the location of the melt may also affect this if the optical fiber sees only a limited portion of the plasma, where the emissions are especially strong or weak. Moreover, it was found by image analysis that the plasma temperature decreases by a few hundred degrees when the plasma stabilizes and when the reduction degree is high.

The information provided in this article can be used in planning future measurement campaigns. For example, the distinct slag components in the fluxed hematite spectra and the connection between the arc length and the electron density can be useful when scaling up the process. The results obtained can also be used to validate semi-empirical and numerical models for optimization of the plasma arc in the HPSR process. The next step would be to conduct more research on varying materials to learn how the emission lines behave with low-grade ores and what can possibly be discovered about the reaction kinetics and the slag composition based on that. Furthermore, OES should be used to study the scaling of the process to pilot and industrial-scale furnaces, to make HPSR a suitable process for commercial furnaces.

ACKNOWLEDGMENTS

The authors gratefully acknowledge the funding from the Horizon Europe under the H2PlasmaRed project no. 101138228, and the University of Oulu and the Research Council of Finland for funding under grant no. 352788 H2FUTURE Profi7. DR acknowledges funding by the European Union through the project ROC, sponsored by the European Research Council (ERC, 567 Grant No. 101054368).

FUNDING

Open Access funding provided by University of Oulu (including Oulu University Hospital).

CONFLICT OF INTEREST

The authors declare that they have no conflict of interest.

REFERENCES

1. G. Wimmer, B. Voraberger, B. Kradel, and A. Fleischanderl: *Tech. Rev. Mitsubishi Heavy Ind.*, 2022, vol. 59(4), p. 1.
2. L. Holappa: *Metals*, 2020, vol. 10(9), p. 1117. https://doi.org/10.3390/met10091117.
3. Iron and Steel Technology Roadmap: *Towards more sustainable steelmaking*, OECD Publishing, International Energy Agency, 2020.
4. World Steel Association: Sustainability Indicators 2023. Accessed 13 November 2024 (2023). https://worldsteel.org/wp-content/uploads/Sustainability-indicators-report-2023.pdf.
5. H.-J. Odenthal, A. Kemminger, F. Krause, L. Sankowski, N. Uebber, and N. Vogl: *Steel Res. Int.*, 2018, vol. 89(1), p. 1700098. https://doi.org/10.1002/srin.201700098.
6. D. Raabe, M. Jovičević-Klug, D. Ponge, A. Gramlich, A.K. Silva, A.N. Grundy, H. Springer, I. Souza Filho, and Y. Ma: *Annu. Rev. Mater. Res.*, 2024, vol. 54(2024), pp. 247–97. https://doi.org/10.1146/annurev-matsci-080222-123648.
7. D. Raabe: *Chem. Rev.*, 2023, vol. 123(5), pp. 2436–2608. https://doi.org/10.1021/acs.chemrev.2c00799.
8. M. Xylia, S. Silveira, J. Duerinck, and F. Meinke-Hubeny: *Energy Effic.*, 2018, vol. 11, pp. 1135–59. https://doi.org/10.1007/s12053-017-9583-7.
9. T. Watari and B. McLellan: *Int. J. Hydrog. Energy*, 2024, vol. 79, pp. 630–35. https://doi.org/10.1016/j.ijhydene.2024.06.423.
10. J. Ling, H. Yang, G. Tian, J. Cheng, X. Wang, and X. Yu: *J. Clean. Prod.*, 2024, vol. 441, 140933https://doi.org/10.1016/j.jclepro.2024.140933.
11. M. Kirschen, T. Hay, and T. Echterhof: *Processes*, 2021, vol. 9(2), p. 402. https://doi.org/10.3390/pr9020402.
12. International Iron Metallics Association: Use of Hot Briquetted Iron (HBI) in the Basic Oxygen Furnace (BOF) for steelmaking. Accessed 7 March 2025 (2025). https://metallics.org/wp-content/uploads/2024/08/IIMA_OBM_Factsheet_3_HBI_BOF_Steelmaking.pdf.
13. I.R. Souza Filho, H. Springer, Y. Ma, A. Mahajan, C.C. Silva, M. Kulse, and D. Raabe: *J. Clean. Prod.*, 2022, vol. 340, p. 130805https://doi.org/10.1016/j.jclepro.2022.130805.
14. D. Ernst, U. Manzoor, I.R. Souza Filho, M.A. Zarl, and J. Schenk: *Metals*, 2023, vol. 13(3), p. 558. https://doi.org/10.3390/met13030558.
15. M.A. Zarl, M.A. Farkas, and J. Schenk: *Metals*, 2020, vol. 10(10), p. 1394. https://doi.org/10.3390/met10101394.
16. M.A. Zarl, D. Ernst, J. Cejka, and J. Schenk: *Materials*, 2022, vol. 15(14), p. 4767. https://doi.org/10.3390/ma15144767.
17. D. Ernst, M.A. Zarl, J. Cejka, and J. Schenk: *Materials*, 2022, vol. 15(12), p. 4065. https://doi.org/10.3390/ma15124065.
18. I.R. Souza Filho, Y. Ma, D. Raabe, and H. Springer: *JOM*, 2023, vol. 75(7), pp. 2274–86. https://doi.org/10.1007/s11837-023-05829-z.
19. M. Naseri Seftejani, J. Schenk, and M.A. Zarl: *Materials*, 2019, vol. 12(10), p. 1608. https://doi.org/10.3390/ma12101608.
20. M. Naseri Seftejani, J. Schenk, D. Spreitzer, and M. Andreas Zarl: *Materials*, 2020, vol. 13(4), p. 935. https://doi.org/10.3390/ma13040935.
21. I.R. Souza Filho, Y. Ma, M. Kulse, D. Ponge, B. Gault, H. Springer, and D. Raabe: *Acta Mater.*, 2021, vol. 213, 116971https://doi.org/10.1016/j.actamat.2021.116971.
22. R. Kannan, A.G. Stevens, C. Fancher, O. Rahman, R. Miller, J. Ward, A.K. Ziabari, S.S. Babu, and P. Nandwana: *Sustain. Mater. Technol.*, 2024, vol. 40, p. 00879. https://doi.org/10.1016/j.susmat.2024.e00879.
23. M. Jovičević-Klug, I.R. Souza Filho, H. Springer, C. Adam, and D. Raabe: *Nature*, 2024, vol. 625(7996), pp. 703–09. https://doi.org/10.1038/s41586-023-06901-z.
24. Z. Zulhan, B. Hakim, Y. Hendrawan, T. Hidayat, E.F. Hermansyah, A.H. Yusro, and A.L.J. Pambudi: *Mater. Res. Technol.*, 2024, vol. 30, pp. 5346–55. https://doi.org/10.1016/j.jmrt.2024.04.205.
25. O.K. Büyükuslu, L.S. Aota, D. Raabe, H. Springer, and I.R. Souza-Filho: *Acta Mater.*, 2024, vol. 277, p. 120221. https://doi.org/10.1016/j.actamat.2024.120221.
26. H. Pauna, T. Willms, M. Aula, T. Echterhof, M. Huttula, and T. Fabritius: *Plasma Res. Express*, 2019, vol. 1(3), 035007https://doi.org/10.1088/2516-1067/ab30dd.
27. H. Pauna, M. Aula, J. Seehausen, J.-S. Klung, M. Huttula, and T. Fabritius: *Steel Res. Int.*, 2020, vol. 91(11), p. 2000051. https://doi.org/10.1002/srin.202000051.
28. H. Pauna, A. Tuomela, M. Aula, P. Turunen, V. Pankratov, M. Huttula, and T. Fabritius: *Metall. Mater. Trans. B*, 2022, vol. 53B, pp. 454–65. https://doi.org/10.1007/s11663-021-02382-5.
29. H. Pauna, D. Ernst, M. Zarl, M. Aula, J. Schenk, M. Huttula, and T. Fabritius: *J. Clean. Prod.*, 2022, vol. 372, 133755https://doi.org/10.1016/j.jclepro.2022.133755.
30. H. Pauna, D. Ernst, M. Zarl, I.R. Souza Filho, M. Kulse, O. Büyükuslu, M. Jovičević-Klug, H. Springer, M. Huttula, J. Schenk, T. Fabritius, and D. Raabe: *Steel Res. Int.*, 2024, vol. 95, 2400028. https://doi.org/10.1002/srin.202400028.
31. A.J. Muwanguzi, A.V. Karasev, J.K. Byaruhanga, and P.G. Jönsson: *Int. Scholarly Res. Not.*, 2012, vol. 2012(1), p. 174803. https://doi.org/10.5402/2012/174803.
32. A. Kramida, Yu. Ralchenko, J. Reader, and NIST ASD Team: NIST Atomic Spectra Database (ver. 5.11). [Online],30 September 2024. National Institute of Standards and Technology, Gaithersburg, 2023. Available: https://physics.nist.gov/asd.
33. R.D.Cowan: *The Theory of Atomic Structure and Spectra*. University of California Press, Berkeley, 1981, p. 22.
34. D. Bulajic, M. Corsi, G. Cristoforetti, S. Legnaioli, V. Palleschi, A. Salvetti, and E. Tognoni: *Spectrochim. Acta Part B*, 2002, vol. 57(2), pp. 339–53. https://doi.org/10.1016/S0584-8547(01)00398-6.

35. F. Colao, R. Fantoni, V. Lazic, and A. Paolini: *Appl. Phys. A Mater. Sci. Process.*, 2004, vol. 79, pp. 143–52. https://doi.org/10.1007/s00339-003-2262-x.
36. A. El Sherbini, T.M. El Sherbini, H. Hegazy, G. Cristoforetti, S. Legnaioli, V. Palleschi, L. Pardini, A. Salvetti, and E. Tognoni: *Spectrochim. Acta Part B*, 2005, vol. 60(12), pp. 1573–79. https://doi.org/10.1016/j.sab.2005.10.011.
37. C. Aragón and J.A. Aguilera: *Spectrochim. Acta B*, 2008, vol. 63(9), pp. 893–916. https://doi.org/10.1016/j.sab.2008.05.010.
38. D. Surmick and C. Parigger: *Int. Rev. At. Mol. Phys*, 2014, vol. 5, pp. 73–81.
39. S. Das, D.P. Das, P. Rajput, J. Ghosh, B. Bhoi, and B.K. Mishra: *Plasma Chem. Plasma Process.*, 2016, vol. 36, pp. 1125–39. https://doi.org/10.1007/s11090-016-9705-6.
40. A. Rautioaho, H. Pauna, V.-V. Visuri, M. Huttula, and T. Fabritius: *IOP Conf. Ser. Mater. Sci. Eng.*, 2024, vol. 1309, 012-001https://doi.org/10.1088/1757-899X/1309/1/012001.
41. M. Aula, A. Leppänen, J. Roininen, E.-P. Heikkinen, K. Vallo, T. Fabritius, and M. Huttula: *Metall. Mater. Trans. B*, 2014, vol. 45B, pp. 839–49. https://doi.org/10.1007/s11663-014-0032-0.
42. Luxmet: ArcSpec - Luxmet. Accessed 19 February 2025. https://www.luxmet.fi/arcspec/.